A 27-node hybrid brick and a 21-node hybrid wedge element for structural analysis

C.S. Jog*

Department of Mechanical Engineering, Indian Institute of Science, Bangalore 560012, India

Abstract

This paper presents a 27-node hybrid hexahedral and a 21-node hybrid wedge element for structural analysis. The motivation behind developing these elements is that, in many situations, it is convenient to use elements that involve only displacement degrees of freedom as in a standard displacement-based brick element, but, in order that computational costs are not prohibitively high, such elements should perform well irrespective of whether they are used to model three-dimensional or plate/shell geometries, whether the material is compressible or almost incompressible and so on. In other words, it is desirable to develop elements that are simple to use, but at the same time extremely versatile in modeling a wide range of geometries, material behavior, etc. The formulation of the proposed elements is based on a two-field mixed variational principle. The higher-order terms in the stress interpolation are identified based on the zero-energy modes that can occur in cubical and wedge-shaped elements, respectively. The resulting elements are "optimal" in the sense that they have the minimum number of assumed stress terms to ensure correct stiffness rank. Numerical examples are presented to show the excellent performance of the proposed elements under demanding situations such as when the elements are used to model plate/shell geometries, when the material is almost incompressible, the meshes are distorted, etc.

Keywords: Hybrid brick and wedge elements; Structural analysis

1. Introduction

Hybrid finite elements are known to be one of the most accurate class of finite elements. In particular, they are relatively insensitive to mesh distortion as compared to displacement-based elements,

* Tel.: +91 80 22932957; fax: +91 80 23600648.
E-mail address: jogc@mecheng.iisc.ernet.in.

and work well even when the material is almost incompressible. Moreover, the classical hybrid elements, being essentially two-field mixed finite elements with the stress (or strain) degrees of freedom condensed out, are also very convenient from a user-viewpoint, since the degrees of freedom (and hence, the input data) that the user works with are exactly as in a conventional single-field displacement-based formulation.

Although there are several formulations of 20/21 node three-dimensional hybrid brick elements, which can be considered as natural extensions of the 8-node planar element, (see, e.g., [1–5]), to the best of our knowledge, there seems to have been no work on the development of the natural extension of a 9-node planar element, namely, a 27-node three-dimensional hybrid brick element. Just as a standard displacement-based 9-node planar element offers several advantages over the corresponding 8-node element with a small incremental increase in cost, one expects the 27-node hybrid element to be more robust compared to its 20-node counterparts. Another possible advantage is that an existing mesh of 8-noded brick elements can be used to construct a mesh of 27-node elements by "clubbing" together eight 8-node elements to form a single 27-node element. We also develop a 21-node wedge element in this work since it is convenient to mesh circular plates or hemispheres with a combination of wedge and brick elements, with the wedge elements being used in the layer adjacent to the center.

In many applications, one needs to analyze a body comprising of one or multiple thin shells connected to a solid body; if the shell part is modeled by shell elements, and the solid part by solid brick elements, then special transition elements are required to match the rotational degrees of freedom of the shell elements with the translational degrees of freedom of the solid elements. Ideally, in such a case, one would like to model the entire structure using brick elements without, of course, having to use a very refined mesh for modeling the shell part. The rotational degrees of freedom also makes the design of shell elements extremely complicated, especially in large-deformation problems [6]. Comparatively speaking, the design of brick elements is simpler, although the disadvantages that they suffer from when used to model shell structures are that

1. unless special strategies are used, membrane or shear locking can occur,
2. an integration through the thickness has to be carried out, which, at least in shell elements based on Cosserat models, can be avoided.

Based on the above considerations, what one would like to have is elements which not only work well when used to model three-dimensional geometries, but which are also relatively immune from locking when used to model plate/shell geometries. This is the motivation for the development of the 27-node brick and 21-node wedge elements in this work. Indeed, as we show in Section 3, the proposed elements yield very good accuracy even with coarse meshes on demanding problems involving doubly-curved shells, severe mesh distortions, incompressible materials, etc., and in particular, result in a significant increase in accuracy in pathological situations where lower-order hybrid elements yield poor results.

We note the convention that is followed throughout this work. Scalars are denoted by lightface letters, while vectors and higher-order tensors are denoted by boldface letters. The dot symbol is used to denote contraction over one index, while the colon symbol is used to denote contraction over two indices. For example, $\boldsymbol{t} \cdot \boldsymbol{u} = t_i u_i$, $\boldsymbol{\tau} : \boldsymbol{\epsilon} = \tau_{ij} \varepsilon_{ij}$, etc., with the summation convention over repeated indices implied.

2. Formulation

Before proceeding to the development of the finite element formulation, we briefly outline the development of the underlying variational equations for the sake of future reference. Let Ω be an open domain whose boundary Γ is composed of two open, disjoint regions, $\Gamma = \overline{\Gamma_u \cup \Gamma_t}$. We are interested in finding an approximate numerical solution to the following boundary value problem of linearized elasticity:

Find the displacements $\boldsymbol{u}$, stresses $\boldsymbol{\tau}$, strains $\boldsymbol{\epsilon}$, and tractions $\boldsymbol{t}$, such that

$$\boldsymbol{\nabla} \cdot \boldsymbol{\tau} + \boldsymbol{b} = \boldsymbol{0} \quad \text{on } \Omega, \tag{1}$$

$$\boldsymbol{\tau} = \mathbf{C} : \boldsymbol{\epsilon} \quad \text{on } \Omega, \tag{2}$$

$$\boldsymbol{\epsilon} = \tfrac{1}{2}\left[(\boldsymbol{\nabla u}) + (\boldsymbol{\nabla u})^t\right] \quad \text{on } \Omega, \tag{3}$$

$$\boldsymbol{t} = \boldsymbol{\tau} \cdot \boldsymbol{n} \quad \text{on } \Gamma, \tag{4}$$

$$\boldsymbol{t} = \bar{\boldsymbol{t}} \quad \text{on } \Gamma_t, \tag{5}$$

$$\boldsymbol{u} = \boldsymbol{0} \quad \text{on } \Gamma_u, \tag{6}$$

where $\boldsymbol{n}$ is the outward normal to Γ, and $\bar{\boldsymbol{t}}$ are the prescribed tractions on Γ_t.

Let

$$V_u = \{v_i \in H^1(\Omega),\ i = 1,3 :\ \boldsymbol{v} = \boldsymbol{0} \text{ on } \Gamma_u\},$$

$$V_\tau = \{\sigma_{ij} \in L^2(\Omega),\ i, j = 1,3 :\ \boldsymbol{\sigma} = \boldsymbol{\sigma}^t\},$$

and let the function $\bar{\boldsymbol{\epsilon}}$ be defined as

$$\bar{\boldsymbol{\epsilon}}(\boldsymbol{z}) := \tfrac{1}{2}\left[\boldsymbol{\nabla z} + (\boldsymbol{\nabla z})^t\right]. \tag{7}$$

Our hybrid finite element formulation is based on the variational statements obtained by enforcing Eqs. (1), (3) and (5) in a weak sense, with the remaining equations enforced in a strong (or pointwise) sense. Thus, if $(\boldsymbol{v}, \boldsymbol{\sigma}) \in (V_u \times V_\tau)$ denote the variations of the displacement and stress fields respectively, then the weak enforcement of the aforementioned equations yields

$$\int_\Omega \boldsymbol{v} \cdot (\boldsymbol{\nabla} \cdot \boldsymbol{\tau} + \boldsymbol{b})\, \mathrm{d}\Omega + \int_{\Gamma_t} \boldsymbol{v} \cdot (\bar{\boldsymbol{t}} - \boldsymbol{t})\, \mathrm{d}\Gamma + \int_\Omega \boldsymbol{\sigma} : [\bar{\boldsymbol{\epsilon}}(\boldsymbol{u}) - \mathbf{C}^{-1} : \boldsymbol{\tau}]\, \mathrm{d}\Omega = 0 \quad \forall (\boldsymbol{v}, \boldsymbol{\sigma}) \in (V_u \times V_\tau). \tag{8}$$

By using the identity $\boldsymbol{\nabla} \cdot (\boldsymbol{\tau}^t \cdot \boldsymbol{v}) = \boldsymbol{v} \cdot (\boldsymbol{\nabla} \cdot \boldsymbol{\tau}) + \boldsymbol{\nabla v} : \boldsymbol{\tau}$, the symmetry of $\boldsymbol{\tau}$ and the divergence theorem, and then successively considering the two cases $(\boldsymbol{v}, \boldsymbol{\sigma}) = (\boldsymbol{0}, \boldsymbol{\sigma})$ and $(\boldsymbol{v}, \boldsymbol{\sigma}) = (\boldsymbol{v}, \boldsymbol{0})$, the above equation simplifies to

$$\int_\Omega \boldsymbol{\sigma}_c^t [\bar{\boldsymbol{\epsilon}}_c(\boldsymbol{u}) - \boldsymbol{C}^{-1} \boldsymbol{\tau}_c]\, \mathrm{d}\Omega = 0 \quad \forall \boldsymbol{\sigma}_c, \tag{9}$$

$$\int_\Omega [\bar{\boldsymbol{\epsilon}}_c(\boldsymbol{v})]^t \boldsymbol{\tau}_c\, \mathrm{d}\Omega = \int_\Omega \boldsymbol{v}^t \boldsymbol{b}\, \mathrm{d}\Omega + \int_{\Gamma_t} \boldsymbol{v}^t \bar{\boldsymbol{t}}\, \mathrm{d}\Gamma \quad \forall \boldsymbol{v} \in V_u, \tag{10}$$

where $(\bar{\boldsymbol{\epsilon}}_c)_{6\times 1}$, $(\boldsymbol{\tau}_c)_{6\times 1}$ and $\boldsymbol{C}_{6\times 6}$ denote the function given by Eq. (7), the stress tensor, and the material constitutive tensors expressed in "vector" form.

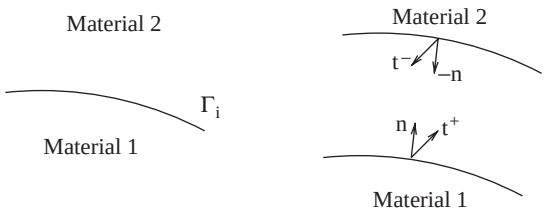

Fig. 1. The traction continuity condition, $\boldsymbol{t}^+ + \boldsymbol{t}^- = \boldsymbol{0}$, at a bi-material interface.

Consider now the case when the body is composed of two or more materials as shown in Fig. 1. The governing equations (1)–(3) are valid within each material subdomain, and the Cauchy relation given by Eq. (4) holds at the interface Γ_i in addition to the outer boundary. The boundary conditions at the interface Γ_i are that both the displacements and tractions be continuous. If, similar to the traction boundary condition on Γ_t, the continuity of tractions at Γ_i is enforced in a *weak* sense, then the term $-\int_{\Gamma_i} \boldsymbol{v} \cdot (\boldsymbol{t}^+ + \boldsymbol{t}^-)\, \mathrm{d}\Gamma$ gets added to the left-hand side of Eq. (8), and by following the same procedure as above, we again obtain Eqs. (9) and (10). The advantage of implementing the traction continuity condition in a weak rather than a strong sense (as in, e.g., [7]) is that, apart from the requirement that Γ_i coincides with element edges, no change in the finite element formulation is required while modeling composite materials.

Let the displacement and stress fields, and their variations, be interpolated as

$$\boldsymbol{u} = \boldsymbol{N}\hat{\boldsymbol{u}}, \quad \boldsymbol{\tau}_c = \boldsymbol{P}\hat{\boldsymbol{\beta}},$$

$$\boldsymbol{v} = \boldsymbol{N}\hat{\boldsymbol{v}}, \quad \boldsymbol{\sigma}_c = \boldsymbol{P}\hat{\boldsymbol{\gamma}}.$$

Substituting the above interpolations into Eqs. (9) and (10), and invoking the arbitrariness of $\hat{\boldsymbol{v}}$ and $\hat{\boldsymbol{\gamma}}$, we get the matrix equations

$$\begin{bmatrix} -\boldsymbol{H} & \boldsymbol{G} \\ \boldsymbol{G}^t & \boldsymbol{0} \end{bmatrix} \begin{bmatrix} \hat{\boldsymbol{\beta}} \\ \hat{\boldsymbol{u}} \end{bmatrix} = \begin{bmatrix} \hat{\boldsymbol{g}} \\ \hat{\boldsymbol{f}} \end{bmatrix}, \tag{11}$$

where, with $\boldsymbol{S}$ denoting the material compliance matrix $\boldsymbol{C}^{-1}$, and $\boldsymbol{B}$ denoting the "strain-displacement matrix" (i.e., $\bar{\epsilon}_c = \boldsymbol{B}\hat{\boldsymbol{u}}$),

$$\boldsymbol{H} = \int_\Omega \boldsymbol{P}^t \boldsymbol{S} \boldsymbol{P}\, \mathrm{d}\Omega,$$

$$\boldsymbol{G} = \int_\Omega \boldsymbol{P}^t \boldsymbol{B}\, \mathrm{d}\Omega,$$

$$\hat{\boldsymbol{g}} = \boldsymbol{0},$$

$$\hat{\boldsymbol{f}} = \int_\Omega \boldsymbol{N}_u^t \boldsymbol{b}\, \mathrm{d}\Omega + \int_{\Gamma_t} \boldsymbol{N}_u^t \bar{\boldsymbol{t}}\, \mathrm{d}\Gamma.$$

Eliminating $\hat{\boldsymbol{\beta}}$ in the system of equations given by Eq. (11), we get

$$\boldsymbol{K}\hat{\boldsymbol{u}} = \hat{\boldsymbol{f}}, \tag{12}$$

with

$$\boldsymbol{K} = \boldsymbol{G}^t \boldsymbol{H}^{-1} \boldsymbol{G}.$$

Since the stress interpolation is allowed to be discontinuous across element boundaries, $\boldsymbol{H}^{-1}$ is composed of distinct block matrices $\boldsymbol{H}_{(e)}^{-1}$ associated with each element. Thus, the element stiffness matrix is given by

$$\boldsymbol{K}_{(e)} = \boldsymbol{G}_{(e)}^t \boldsymbol{H}_{(e)}^{-1} \boldsymbol{G}_{(e)}, \tag{13}$$

where, with Ω_e denoting the domain of each element,

$$\boldsymbol{H}_{(e)} = \int_{\Omega_e} \boldsymbol{P}_{(e)}^t \boldsymbol{S} \boldsymbol{P}_{(e)} \, \mathrm{d}\Omega,$$

$$\boldsymbol{G}_{(e)} = \int_{\Omega_e} \boldsymbol{P}_{(e)}^t \boldsymbol{B}_{(e)} \, \mathrm{d}\Omega.$$

Once the displacement field is found using Eq. (12), the stress and strain fields in an element are recovered using the relations

$$\boldsymbol{\tau}_c^{(e)} = \boldsymbol{P}_{(e)} \hat{\boldsymbol{\beta}}_{(e)} = \boldsymbol{P}_{(e)} \boldsymbol{H}_{(e)}^{-1} \boldsymbol{G}_{(e)} \hat{\boldsymbol{u}}_{(e)}, \tag{14a}$$

$$\boldsymbol{\epsilon}_c^{(e)} = \boldsymbol{S} \boldsymbol{\tau}_c^{(e)} = \boldsymbol{S} \boldsymbol{P}_{(e)} \boldsymbol{H}_{(e)}^{-1} \boldsymbol{G}_{(e)} \hat{\boldsymbol{u}}_{(e)}. \tag{14b}$$

As noted in the Introduction, and as evident from Eq. (12), the global equation solving needs to be carried out for the displacement degrees of freedom alone, so that the input data is exactly the same as in a standard single-field displacement-based formulation. Also, similar to a standard single-field displacement-based formulation, the relation $\int_\Omega \boldsymbol{B}^t \boldsymbol{\tau}_c \, \mathrm{d}\Omega = \hat{\boldsymbol{f}}$ holds. We now discuss the formulations of the proposed elements.

2.1. 27-node brick element

The key point in a hybrid formulation is the choice of the stress interpolation matrix $\boldsymbol{P}_{(e)}$, and we now discuss this issue in the context of the 27-node element. It is well known that the necessary condition for the stiffness matrix to have the correct rank is that the number of stress parameters (i.e., the number of parameters in the vector $\hat{\boldsymbol{\beta}}_{(e)}$) should be greater than or equal to the number of displacement degrees of freedom minus the number of rigid-body modes [3]. Thus, since the 27-node element has 81 displacement degrees of freedom, and since there are six rigid body modes, the minimum number of stress parameters required is 75. Since each additional parameter adds more stiffness in addition to increasing the computational cost of inverting $\boldsymbol{H}_{(e)}$, it is desirable to have the minimum number of β's in a hybrid formulation, namely 75 in the context of this element.

To identify the terms in the stress interpolation matrix, consider the strain energy in an element generated by an admissible deformation (i.e., one obtained using the displacement interpolation $\boldsymbol{u}_{(e)} = \boldsymbol{N}_{(e)} \hat{\boldsymbol{u}}_{(e)}$), and given by

$$\frac{1}{2} \hat{\boldsymbol{u}}_{(e)}^t \boldsymbol{K}_{(e)} \hat{\boldsymbol{u}}_{(e)} = \frac{1}{2} \left[\int_{\Omega_e} [\bar{\boldsymbol{\epsilon}}_c(\boldsymbol{u}_{(e)})]^t \boldsymbol{P}_{(e)} \, \mathrm{d}\Omega \right] \boldsymbol{H}_{(e)}^{-1} \left[\int_{\Omega_e} \boldsymbol{P}_{(e)}^t \bar{\boldsymbol{\epsilon}}_c(\boldsymbol{u}_{(e)}) \, \mathrm{d}\Omega \right].$$

From the above expression, we see that fields $\boldsymbol{u}_{(e)}$ (excluding infinitesimal rigid displacements) which are such that

$$\int_{\Omega_e} \boldsymbol{P}^t_{(e)} \bar{\boldsymbol{\epsilon}}_c(\boldsymbol{u}_{(e)})\, \mathrm{d}\Omega = \boldsymbol{0},$$

result in zero strain energy, or equivalently, a singular stiffness matrix, even when the body is constrained so as to disallow rigid motion. The stress interpolation matrix $\boldsymbol{P}_{(e)}$ is chosen so as to prevent such a singularity. A natural choice for the lower-order terms, denoted by $[\boldsymbol{P}_{(e)}]_{\mathrm{L}}$, is

$$[\boldsymbol{P}_{(e)}]_{\mathrm{L}} = [\boldsymbol{I}_6 \;\; \xi\boldsymbol{I}_6 \;\; \eta\boldsymbol{I}_6 \;\; \zeta\boldsymbol{I}_6 \;\; \xi\eta\boldsymbol{I}_6 \;\; \eta\zeta\boldsymbol{I}_6 \;\; \xi\zeta\boldsymbol{I}_6 \;\; \xi\eta\zeta\boldsymbol{I}_6],$$

where $\boldsymbol{I}$ is the identity matrix. To identify the higher-order terms, consider a cubical element whose surfaces are given by $\xi = \pm 1$, $\eta = \pm 1$ and $\zeta = \pm 1$, and consider fields $\bar{\boldsymbol{\epsilon}}_c(\boldsymbol{u}_{(e)})$, obtained from admissible deformations $\boldsymbol{u}_{(e)}$, that vanish at the $2 \times 2 \times 2$ Gauss points of such an element. These fields satisfy the condition

$$\int_{\Omega_e} [\boldsymbol{P}^t_{(e)}]_{\mathrm{L}} \bar{\boldsymbol{\epsilon}}_c(\boldsymbol{u}_{(e)})\, \mathrm{d}\Omega = \boldsymbol{0},$$

since $[\boldsymbol{P}^t_{(e)}]_{\mathrm{L}} \bar{\boldsymbol{\epsilon}}_c(\boldsymbol{u}_{(e)})$ contains polynomial terms that are at most cubic in each of the natural coordinates (ξ, η, ζ), so that the integral in the above equation can be evaluated exactly using a $2 \times 2 \times 2$ Gauss quadrature rule. Thus, the higher-order terms $[\boldsymbol{P}_{(e)}]_{\mathrm{H}}$ should be chosen such that for the same fields $\bar{\boldsymbol{\epsilon}}_c(\boldsymbol{u}_{(e)})$ considered above,

$$\int_{\Omega_e} [\boldsymbol{P}^t_{(e)}]_{\mathrm{H}} \bar{\boldsymbol{\epsilon}}_c(\boldsymbol{u}_{(e)})\, \mathrm{d}\Omega \neq \boldsymbol{0}.$$

The above strategy has been used by Lee et al. [8,9], and subsequently also by Sze et al. [5,10]. However, as has been pointed out (see, e.g., Ref. [3]), several different choices of assumed stress terms can lead to the suppression of the zero-energy modes, and here, we shall present one that we believe (based on numerical experimentation) to be the best choice.

For a cubical element whose surfaces are given by $\xi = \pm 1$, $\eta = \pm 1$ and $\zeta = \pm 1$, the admissible deformations $\boldsymbol{u}_{(e)}$ that yield $\bar{\boldsymbol{\epsilon}}_c(\boldsymbol{u}_{(e)}) = \boldsymbol{0}$ at the $2 \times 2 \times 2$ Gauss quadrature points (whose natural coordinates are given by $(\xi, \eta, \zeta) = (\pm 1/\sqrt{3}, \pm 1/\sqrt{3}, \pm 1/\sqrt{3})$), are

1. $u = \alpha_1(1 - 3\xi^2)(1 - 3\eta^2)$, $v = 0$, $w = 0$,
2. $u = \alpha_2(1 - 3\xi^2)(1 - 3\zeta^2)$, $v = 0$, $w = 0$,
3. $u = \alpha_3\eta(1 - 3\xi^2)(1 - 3\zeta^2)$, $v = 0$, $w = 0$,
4. $u = \alpha_4\zeta(1 - 3\xi^2)(1 - 3\eta^2)$, $v = 0$, $w = 0$,
5. $u = \alpha_5(1 - 3\xi^2)(1 - 3\eta^2)(1 - 3\zeta^2)$, $v = 0$, $w = 0$,
6. $u = 0$, $v = \alpha_6(1 - 3\xi^2)(1 - 3\eta^2)$, $w = 0$,
7. $u = 0$, $v = \alpha_7(1 - 3\eta^2)(1 - 3\zeta^2)$, $w = 0$,
8. $u = 0$, $v = \alpha_8\xi(1 - 3\eta^2)(1 - 3\zeta^2)$, $w = 0$,
9. $u = 0$, $v = \alpha_9\zeta(1 - 3\xi^2)(1 - 3\eta^2)$, $w = 0$,
10. $u = 0$, $v = \alpha_{10}(1 - 3\xi^2)(1 - 3\eta^2)(1 - 3\zeta^2)$, $w = 0$,
11. $u = 0$, $v = 0$, $w = \alpha_{11}(1 - 3\xi^2)(1 - 3\zeta^2)$,
12. $u = 0$, $v = 0$, $w = \alpha_{12}(1 - 3\eta^2)(1 - 3\zeta^2)$,

13. $u = 0$, $v = 0$, $w = \alpha_{13}\xi(1 - 3\eta^2)(1 - 3\zeta^2)$,
14. $u = 0$, $v = 0$, $w = \alpha_{14}\eta(1 - 3\xi^2)(1 - 3\zeta^2)$,
15. $u = 0$, $v = 0$, $w = \alpha_{15}(1 - 3\xi^2)(1 - 3\eta^2)(1 - 3\zeta^2)$,
16. $u = -\alpha_{16}\xi(1 - 3\eta^2)$, $v = \alpha_{16}\eta(1 - 3\xi^2)$, $w = 0$,
17. $u = 0$, $v = -\alpha_{17}\eta(1 - 3\zeta^2)$, $w = \alpha_{17}\zeta(1 - 3\eta^2)$,
18. $u = \alpha_{18}\xi(1 - 3\zeta^2)$, $v = 0$, $w = -\alpha_{18}\zeta(1 - 3\xi^2)$,
19. $u = \alpha_{19}(1 - 3\eta^2)(1 - 3\zeta^2)$, $v = \alpha_{20}(1 - 3\xi^2)(1 - 3\zeta^2)$, $w = 0$,
20. $u = 0$, $v = \alpha_{21}(1 - 3\xi^2)(1 - 3\zeta^2)$, $w = \alpha_{22}(1 - 3\xi^2)(1 - 3\eta^2)$,
21. $u = \alpha_{23}(1 - 3\eta^2)(1 - 3\zeta^2)$, $v = 0$, $w = \alpha_{24}(1 - 3\xi^2)(1 - 3\eta^2)$,
22. $u = \alpha_{25}\xi(1 - 3\eta^2)(1 - 3\zeta^2)$, $v = 0$, $w = 0$,
23. $u = 0$, $v = \alpha_{26}\eta(1 - 3\xi^2)(1 - 3\zeta^2)$, $w = 0$,
24. $u = 0$, $v = 0$, $w = \alpha_{27}\zeta(1 - 3\xi^2)(1 - 3\eta^2)$.

Note that

1. the zero-energy modes

   (a) $u = -\gamma_1\xi\zeta(1 - 3\eta^2)$, $v = \gamma_1\eta\zeta(1 - 3\xi^2)$, $w = 0$,
   (b) $u = 0$, $v = -\gamma_2\eta\xi(1 - 3\zeta^2)$, $w = \gamma_2\zeta\xi(1 - 3\eta^2)$,
   (c) $u = \gamma_3\xi\eta(1 - 3\zeta^2)$, $v = 0$, $w = -\gamma_3\zeta\eta(1 - 3\xi^2)$

   are non-communicable, i.e., they vanish in an assembly of two or more elements. Nevertheless, they are suppressed while suppressing modes (19)–(21)
2. the zero-energy modes

   (a) $u = -\gamma_4\xi\zeta^2(1 - 3\eta^2)$, $v = \gamma_4\eta\zeta^2(1 - 3\xi^2)$, $w = 0$,
   (b) $u = 0$, $v = -\gamma_5\eta\xi^2(1 - 3\zeta^2)$, $w = \gamma_5\zeta\xi^2(1 - 3\eta^2)$,
   (c) $u = \gamma_6\xi\eta^2(1 - 3\zeta^2)$, $v = 0$, $w = -\gamma_6\zeta\eta^2(1 - 3\xi^2)$

   can be obtained by a superposition of some of the listed modes.

Using one 'β term' to suppress one 'α term' in the listed zero-energy modes, the stress distribution is assumed to be

$$\begin{aligned}\tau^{\xi\xi} &= \beta_1 + \beta_7\xi + \beta_{13}\eta + \beta_{19}\zeta + \beta_{25}\xi\eta + \beta_{31}\eta\zeta + \beta_{37}\xi\zeta + \beta_{43}\xi\eta\zeta \\ &\quad + \beta_{49}\xi\eta^2 + \beta_{52}\xi\zeta^2 + \beta_{55}\xi\eta\zeta^2 + \beta_{58}\xi\eta^2\zeta + \beta_{61}\xi\eta^2\zeta^2 + \beta_{64}\eta^2 - \beta_{65}\zeta^2,\end{aligned}$$

$$\begin{aligned}\tau^{\eta\eta} &= \beta_2 + \beta_8\xi + \beta_{14}\eta + \beta_{20}\zeta + \beta_{26}\xi\eta + \beta_{32}\eta\zeta + \beta_{38}\xi\zeta + \beta_{44}\xi\eta\zeta \\ &\quad + \beta_{50}\xi^2\eta + \beta_{53}\eta\zeta^2 + \beta_{56}\xi^2\eta\zeta + \beta_{59}\xi\eta\zeta^2 + \beta_{62}\xi^2\eta\zeta^2 - \beta_{64}\xi^2 + \beta_{66}\zeta^2,\end{aligned}$$

$$\begin{aligned}\tau^{\zeta\zeta} &= \beta_3 + \beta_9\xi + \beta_{15}\eta + \beta_{21}\zeta + \beta_{27}\xi\eta + \beta_{33}\eta\zeta + \beta_{39}\xi\zeta + \beta_{45}\xi\eta\zeta \\ &\quad + \beta_{51}\xi^2\zeta + \beta_{54}\eta^2\zeta + \beta_{57}\xi^2\eta\zeta + \beta_{60}\xi\eta^2\zeta + \beta_{63}\xi^2\eta^2\zeta + \beta_{65}\xi^2 - \beta_{66}\eta^2,\end{aligned}$$

$$\begin{aligned}\tau^{\xi\eta} &= \beta_4 + \beta_{10}\xi + \beta_{16}\eta + \beta_{22}\zeta + \beta_{28}\xi\eta + \beta_{34}\eta\zeta + \beta_{40}\xi\zeta + \beta_{46}\xi\eta\zeta \\ &\quad + \beta_{67}\xi\zeta^2 + \beta_{70}\eta\zeta^2 + \beta_{73}\xi\eta\zeta^2,\end{aligned}$$

$$\tau^{\eta\zeta} = \beta_5 + \beta_{11}\xi + \beta_{17}\eta + \beta_{23}\zeta + \beta_{29}\xi\eta + \beta_{35}\eta\zeta + \beta_{41}\xi\zeta + \beta_{47}\xi\eta\zeta + \beta_{68}\xi^2\eta + \beta_{71}\xi^2\zeta + \beta_{74}\xi^2\eta\zeta,$$

$$\tau^{\xi\zeta} = \beta_6 + \beta_{12}\xi + \beta_{18}\eta + \beta_{24}\zeta + \beta_{30}\xi\eta + \beta_{36}\eta\zeta + \beta_{42}\xi\zeta + \beta_{48}\xi\eta\zeta + \beta_{69}\xi\eta^2 + \beta_{72}\eta^2\zeta + \beta_{75}\xi\eta^2\zeta.$$

We express the above equations in compact form as

$$\begin{bmatrix} \tau^{\xi\xi} \\ \tau^{\eta\eta} \\ \tau^{\zeta\zeta} \\ \tau^{\xi\eta} \\ \tau^{\eta\zeta} \\ \tau^{\xi\zeta} \end{bmatrix} = [\boldsymbol{I}_6 \mid \boldsymbol{N}_\tau]\,\hat{\boldsymbol{\beta}}_{(e)}, \tag{15}$$

where $\hat{\boldsymbol{\beta}}_{(e)}$ is a 75×1 vector.

In order to obtain the Cartesian components in a manner such that patch test requirements are not violated,[1] we use an idea that has been used in [11,12], namely, to transform all the *non-constant* terms using the actual Jacobian. The advantage of using this strategy is that we get high accuracy and the resultant element passes the patch test. If the Jacobian matrix is given by

$$\boldsymbol{J} = \begin{bmatrix} \dfrac{\partial x}{\partial \xi} & \dfrac{\partial y}{\partial \xi} & \dfrac{\partial z}{\partial \xi} \\ \dfrac{\partial x}{\partial \eta} & \dfrac{\partial y}{\partial \eta} & \dfrac{\partial z}{\partial \eta} \\ \dfrac{\partial x}{\partial \zeta} & \dfrac{\partial y}{\partial \zeta} & \dfrac{\partial z}{\partial \zeta} \end{bmatrix} \equiv \begin{bmatrix} a_1 & b_1 & c_1 \\ a_2 & b_2 & c_2 \\ a_3 & b_3 & c_3 \end{bmatrix},$$

then the transformation relation between the stress components expressed with respect to the natural and Cartesian coordinate systems is given by [3]

$$\begin{bmatrix} \tau_{xx} \\ \tau_{yy} \\ \tau_{zz} \\ \tau_{xy} \\ \tau_{yz} \\ \tau_{xz} \end{bmatrix} = \boldsymbol{A} \begin{bmatrix} \tau^{\xi\xi} \\ \tau^{\eta\eta} \\ \tau^{\zeta\zeta} \\ \tau^{\xi\eta} \\ \tau^{\eta\zeta} \\ \tau^{\xi\zeta} \end{bmatrix}, \tag{16}$$

[1] See also the discussion towards the end of Example 3.6.

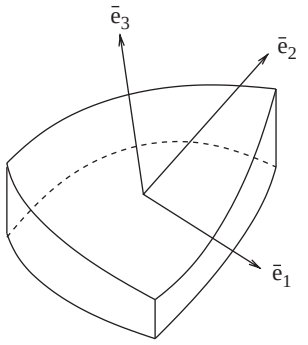

Fig. 2. Geometry of the wedge element, and the local Cartesian coordinate system $\bar{\boldsymbol{e}}_1, \bar{\boldsymbol{e}}_2, \bar{\boldsymbol{e}}_3$ at $(1/3, 1/3, 0)$.

where

$$\boldsymbol{A} = \begin{bmatrix} a_1^2 & a_2^2 & a_3^2 & 2a_1a_2 & 2a_2a_3 & 2a_1a_3 \\ b_1^2 & b_2^2 & b_3^2 & 2b_1b_2 & 2b_2b_3 & 2b_1b_3 \\ c_1^2 & c_2^2 & c_3^2 & 2c_1c_2 & 2c_2c_3 & 2c_1c_3 \\ a_1b_1 & a_2b_2 & a_3b_3 & (a_2b_1 + a_1b_2) & (a_2b_3 + a_3b_2) & (a_1b_3 + a_3b_1) \\ b_1c_1 & b_2c_2 & b_3c_3 & (b_2c_1 + b_1c_2) & (b_2c_3 + b_3c_2) & (b_1c_3 + b_3c_1) \\ a_1c_1 & a_2c_2 & a_3c_3 & (a_1c_2 + a_2c_1) & (a_3c_2 + a_2c_3) & (a_3c_1 + a_1c_3) \end{bmatrix}.$$

Combining Eqs. (15) and (16) (which, as mentioned above, is used only for the non-constant part of the stress tensor), the stress interpolation matrix is given by

$$\boldsymbol{P}_{(e)} = \left[\boldsymbol{I}_6 \;\middle|\; \frac{1}{|\boldsymbol{J}_0|^{2/3}} \boldsymbol{A}\boldsymbol{N}_\tau \right]. \tag{17}$$

The non-dimensionalising factor $|\boldsymbol{J}_0|^{2/3}$, where $|\boldsymbol{J}_0|$ denotes the determinant of the Jacobian evaluated at the parametric center of the element, is introduced to reduce round-off errors, but otherwise, *does not* influence the solution, since its introduction amounts to a scaling (and hence a redefinition) of the β's, which, in any case, are unknowns to be solved for. The above matrix is used in Eq. (13) to form the element stiffness matrix, and then, during postprocessing, in Eqs. (14) to recover the stresses and strains.

2.2. 21-node wedge element

As mentioned in the Introduction, wedge elements are convenient to mesh regions close to the center of a circular plate or hemisphere. A 6-node wedge element has been developed in [13], and here, we extend their ideas to develop a 21-node wedge element which can be used in conjunction with the 27-node brick element discussed in the previous subsection.

As in [13], we use a formulation in terms of a local Cartesian coordinate system (see Fig. 2) instead of one in terms of natural coordinates in order to obtain element invariance. Let (ξ, η, ζ) denote the natural coordinates of the element, with ζ as the transverse direction. We establish the local Cartesian coordinate

system using a procedure similar to that used in [11], and given by

$$\bar{\boldsymbol{e}}_3 = \frac{\dfrac{\partial \boldsymbol{x}}{\partial \zeta}}{\left\| \dfrac{\partial \boldsymbol{x}}{\partial \zeta} \right\|}, \quad \bar{\boldsymbol{e}}_1 = \begin{bmatrix} 1 - \dfrac{(\bar{\boldsymbol{e}}_3)_1^2}{1+(\bar{\boldsymbol{e}}_3)_3} \\ -\dfrac{(\bar{\boldsymbol{e}}_3)_1(\bar{\boldsymbol{e}}_3)_2}{1+(\bar{\boldsymbol{e}}_3)_3} \\ -(\bar{\boldsymbol{e}}_3)_1 \end{bmatrix}, \quad \bar{\boldsymbol{e}}_2 = \begin{bmatrix} -\dfrac{(\bar{\boldsymbol{e}}_3)_1(\bar{\boldsymbol{e}}_3)_2}{1+(\bar{\boldsymbol{e}}_3)_3} \\ 1 - \dfrac{(\bar{\boldsymbol{e}}_3)_2^2}{1+(\bar{\boldsymbol{e}}_3)_3} \\ -(\bar{\boldsymbol{e}}_3)_2 \end{bmatrix}. \tag{18}$$

The shape functions of the 21-node element, denoted by $\tilde{N}_i$, are obtained by using appropriate products of the in-plane shape functions $\bar{N}_i$, $i=1, 2, \ldots, 7$ and the transverse shape functions $L_1(\zeta)=-\zeta(1-\zeta)/2$, $L_2(\zeta) = (1-\zeta^2)$ and $L_3(\zeta) = \zeta(1+\zeta)/2$, where

$$\begin{aligned}
N_1 &= \xi(2\xi-1), & \tilde{N}_1 &= N_1 + 3N_b,\\
N_2 &= \eta(2\eta-1), & \tilde{N}_2 &= N_2 + 3N_b,\\
N_3 &= \rho(2\rho-1), & \tilde{N}_3 &= N_3 + 3N_b,\\
N_4 &= 4\xi\eta, & \tilde{N}_4 &= N_4 - 12N_b,\\
N_5 &= 4\rho\eta, & \tilde{N}_5 &= N_5 - 12N_b,\\
N_6 &= 4\xi\rho, & \tilde{N}_6 &= N_6 - 12N_b,\\
& & \tilde{N}_7 &= 27N_b.
\end{aligned}$$

with the bubble mode $N_b = \xi\eta(1-\xi-\eta)$. If $[\bar{\boldsymbol{x}}] \equiv (\bar{x}, \bar{y}, \bar{z})$ and $[\boldsymbol{x}]$ denote the coordinates of a point with respect to the local and global Cartesian coordinates systems, then they are related by $[\bar{\boldsymbol{x}}] = \boldsymbol{Q}[\boldsymbol{x} - \boldsymbol{x}_0]$, where $\boldsymbol{x}_0$ is the position vector of the origin of the local Cartesian coordinate system, and $\boldsymbol{Q}$ is a proper orthogonal matrix given by

$$\boldsymbol{Q} = \begin{bmatrix} \bar{\boldsymbol{e}}_1 \\ \bar{\boldsymbol{e}}_2 \\ \bar{\boldsymbol{e}}_3 \end{bmatrix}.$$

Thus, knowing the global coordinates at any location (such as a Gauss point) obtained using the interpolation $\sum \tilde{N}_i \boldsymbol{x}_i$, the coordinates with respect to the local coordinate system can be easily recovered using the above formula. Now using a procedure similar to the one used in deriving the stress interpolation matrix for the brick element and in [13], we obtain

$$\begin{aligned}
\tau^{\bar{x}\bar{x}} &= \beta_1 + \beta_7\bar{x} + \beta_{13}\bar{y} + \beta_{19}\frac{\partial \hat{N}_b}{\partial \bar{x}} + \beta_{25}\zeta + \beta_{31}\bar{x}\zeta + \beta_{37}\bar{y}\zeta + \beta_{40}\zeta\frac{\partial \hat{N}_b}{\partial \bar{x}}\\
&\quad + \beta_{43}\zeta^2 + \beta_{46}\bar{x}\zeta^2 + \beta_{49}\bar{y}\zeta^2 + \beta_{52}\zeta^2\frac{\partial \hat{N}_b}{\partial \bar{x}},\\
\tau^{\bar{y}\bar{y}} &= \beta_2 + \beta_8\bar{x} + \beta_{14}\bar{y} + \beta_{20}\frac{\partial \hat{N}_b}{\partial \bar{y}} + \beta_{26}\zeta + \beta_{32}\bar{x}\zeta + \beta_{38}\bar{y}\zeta + \beta_{41}\zeta\frac{\partial \hat{N}_b}{\partial \bar{y}}\\
&\quad + \beta_{44}\zeta^2 + \beta_{47}\bar{x}\zeta^2 + \beta_{50}\bar{y}\zeta^2 + \beta_{53}\zeta^2\frac{\partial \hat{N}_b}{\partial \bar{y}},\\
\tau^{\bar{z}\bar{z}} &= \beta_3 + \beta_9\bar{x} + \beta_{15}\bar{y} + \beta_{21}\bar{x}^2 + \beta_{27}\bar{x}\bar{y} + \beta_{33}\bar{y}^2 + \beta_{39}\hat{N}_b + \beta_{42}\zeta\\
&\quad + \beta_{45}\bar{x}\zeta + \beta_{48}\bar{y}\zeta + \beta_{51}\bar{x}^2\zeta + \beta_{54}\bar{y}^2\zeta + \beta_{55}\bar{x}\bar{y}\zeta + \beta_{56}\zeta\hat{N}_b,
\end{aligned} \tag{19}$$

$$\tau^{\bar{x}\bar{y}} = \beta_4 + \beta_{10}\bar{x} + \beta_{16}\bar{y} + \beta_{22}\zeta + \beta_{28}\bar{x}\zeta + \beta_{34}\bar{y}\zeta,$$

$$\tau^{\bar{y}\bar{z}} = \beta_5 + \beta_{11}\bar{x} + \beta_{17}\bar{y} + \beta_{23}\zeta + \beta_{29}\bar{x}\zeta + \beta_{35}\bar{y}\zeta + \beta_{57}\frac{\partial \hat{N}_b}{\partial \bar{y}},$$

$$\tau^{\bar{x}\bar{z}} = \beta_6 + \beta_{12}\bar{x} + \beta_{18}\bar{y} + \beta_{24}\zeta + \beta_{30}\bar{x}\zeta + \beta_{36}\bar{y}\zeta + \beta_{57}\frac{\partial \hat{N}_b}{\partial \bar{x}},$$

where $\hat{N}_b = \bar{x}\bar{y}(\bar{x} + \bar{y})$. Note that as in the case of the brick element, we use the minimum number of assumed stress terms in order to ensure correct stiffness rank. The transformation of the stress components to the global coordinate system (with, again, only the non-constant part being transformed in order to meet patch test requirements) is carried out as in the case of the brick element with the Jacobian matrix $\boldsymbol{J}$ now given by $\boldsymbol{Q}$.

In the above development, we have used a local Cartesian system at the center of the element in order to develop the element formulation. An alternative choice which we have implemented is to establish an orthogonal curvilinear coordinate system at *every* point in the element, with $\bar{\boldsymbol{e}}_3$ now given by $\boldsymbol{x}_{,\xi} \times \boldsymbol{x}_{,\eta}/\|\boldsymbol{x}_{,\xi} \times \boldsymbol{x}_{,\eta}\|$, and $\bar{\boldsymbol{e}}_1$ and $\bar{\boldsymbol{e}}_2$ given by Eq. (18). The coordinates $(\bar{x}, \bar{y}, \bar{z})$ in this orthogonal curvilinear system are determined via the equations

$$\frac{\partial \bar{x}}{\partial \xi} = \bar{\boldsymbol{e}}_1 \cdot \frac{\partial \boldsymbol{x}}{\partial \xi}, \quad \frac{\partial \bar{y}}{\partial \xi} = \bar{\boldsymbol{e}}_2 \cdot \frac{\partial \boldsymbol{x}}{\partial \xi}, \quad \frac{\partial \bar{z}}{\partial \xi} = 0,$$

$$\frac{\partial \bar{x}}{\partial \eta} = \bar{\boldsymbol{e}}_1 \cdot \frac{\partial \boldsymbol{x}}{\partial \eta}, \quad \frac{\partial \bar{y}}{\partial \eta} = \bar{\boldsymbol{e}}_2 \cdot \frac{\partial \boldsymbol{x}}{\partial \eta}, \quad \frac{\partial \bar{z}}{\partial \eta} = 0,$$

$$\frac{\partial \bar{x}}{\partial \zeta} = \bar{\boldsymbol{e}}_1 \cdot \frac{\partial \boldsymbol{x}}{\partial \zeta}, \quad \frac{\partial \bar{y}}{\partial \zeta} = \bar{\boldsymbol{e}}_2 \cdot \frac{\partial \boldsymbol{x}}{\partial \zeta}, \quad \frac{\partial \bar{z}}{\partial \zeta} = \bar{\boldsymbol{e}}_3 \cdot \frac{\partial \boldsymbol{x}}{\partial \zeta},$$

subject to some "boundary conditions" which determine the integration constants for the above equations, say $\bar{x}(1/3, 1/3, 0) = \bar{y}(1/3, 1/3, 0) = \bar{z}(1/3, 1/3, 0) = 0$. Since there is no known analytical way of determining $(\bar{x}, \bar{y}, \bar{z})$ from the above equations for any arbitrary curved surface, they have to be determined numerically, and then used in the stress interpolation matrix given by Eq. (19). Quite unfortunately, besides the fact that a 60×60 matrix needs to be inverted to determine $(\bar{x}, \bar{y}, \bar{z})$ (in addition to the 57×57 $\boldsymbol{H}$ matrix), the resulting matrices are slightly overstiff. Hence, although, theoretically, this approach is more appealing, the formulation based on a Cartesian system at the center of the element seems to be both more economical and more accurate.

Although, the formation of the element stiffness matrices of the brick and wedge elements discussed above require an inversion of a 75×75 and a 57×57 matrix, respectively, one can reduce the computational cost by following the suggestions of Spilker and Singh [4], namely (1) exploiting the symmetry of $\boldsymbol{H}$, (2) forming $\boldsymbol{H}^{-1}\boldsymbol{G}$, not by explicitly inverting $\boldsymbol{H}$, but by solving the system $\boldsymbol{Hq} = \boldsymbol{G}$ for $\boldsymbol{q}$, and (3) skipping multiplications involving zero terms in $\boldsymbol{S}$ and $\boldsymbol{B}$. Yet another strategy would be to exploit the fact that element stiffness computations can be carried out independent of each other, and thus parallelize the process of constructing element stiffness matrices. As we show in the following section, relatively fewer elements can achieve a given level of accuracy even in demanding problems such as, for example, ones involving doubly curved shell geometries, or almost incompressible materials, and this, we believe, offsets the disadvantage of the higher cost of element stiffness formation.

3. Numerical examples

In this section, we present several examples (many of which have been proposed as test problems in [14]), to show the high accuracy and convergence rate of the proposed elements. We shall compare the solutions obtained using our elements, which we shall refer to as PT75β and W21, with those obtained by using the classical Pian-Tong PT18β element [15], and the 6-node wedge element (denoted by W6) of Sze et al. [13], and in some cases also with the corresponding isoparametric elements denoted by I27 and I21. To ensure a fair comparison of the results, meshes with the *same number of global degrees of freedom* are used, e.g., on any given problem involving hexahedral elements, results obtained using $8N$ PT18β elements are compared against the results obtained using N PT75β elements, with identical nodal coordinate data and boundary conditions used in both meshes. Uniform meshes are used unless otherwise stated. In plate or shell problems, one PT75β element/two PT18β elements are used along the thickness direction, except in the multilayer composite plate problem, where one PT75β element/two PT18β elements per layer are used. Full integration, i.e., $3 \times 3 \times 3$ and 7×3 Gauss quadrature, is used to evaluate all the integrals arising in the formulation of the brick and wedge elements, respectively, and double precision is used in our numerical implementation.

3.1. Patch and eigenvalue test

Since the constant stress modes are explicity provided in the formulation of both elements, they pass the patch test. A cube subdivided into eight distorted elements was used to conduct the patch tests for the PT75β element, while a circular cylinder with wedge elements near to the center was used to conduct the patch tests for the W21 element. The element stiffness matrices have six zero eigenvalues corresponding to the rigid-body modes, thus confirming that the element stiffness matrices are of correct rank. In addition, both elements are coordinate frame invariant.

3.2. Straight and curved beam

A straight cantilever beam and a curved beam (see Figs. 3 and 4), both of thickness 0.1, and with material properties $E = 10^7$, $\nu = 0.3$, and $E = 10^7$, $\nu = 0.25$, respectively, are loaded by a unit in-plane and out-of-plane force at the free end. Both beams are modeled by $6 \times 2 \times 2$ PT18β and by $3 \times 1 \times 1$ PT75β elements. The theoretical tip deflections [14], in the direction of the load in the case of the straight beam for the in-plane and out-of-plane loadings are 0.1081 and 0.4321, while the corresponding figures for the curved beam are 0.08734 and 0.5022. The normalized solutions for the in-plane and out-of plane loadings are shown in Table 1. One observes severe "trapezoidal locking" in the case of the PT18β element, and an improvement in the results for this case by more than an order of magnitude with the use of the PT75β element.

3.3. Clamped rectangular plate

The purpose of this example is to see if shear locking occurs as the thickness h of a plate is reduced in comparison to its lateral dimensions, and also to examine the effect of aspect ratio on the performance. A rectangular plate of lateral dimensions $2a \times 2b$ is subjected to a central point load F; due to symmetry,

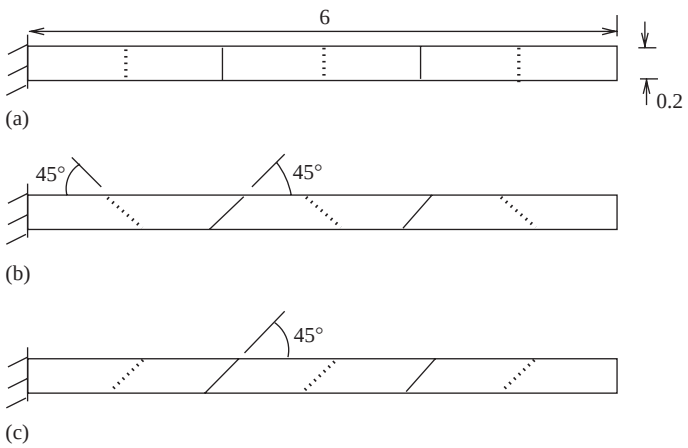

Fig. 3. Straight cantilever beam problem: the beam is shown modeled using three PT75β elements with a dotted line shown joining the midnodes, (a) regular shape elements, (b) trapezoidal shape elements, (c) parallelogram shape elements.

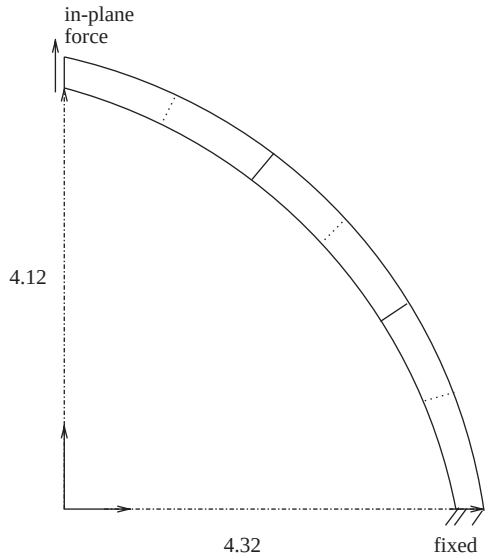

Fig. 4. Curved beam problem: the beam is shown modeled with three uniform PT75β elements with a dotted line shown joining the midnodes.

only a quadrant is modeled as shown in Fig. 5. The material properties are $E = 2.1 \times 10^9$, $v = 0.3$. Meshes of $4 \times 4 \times 2$ and $8 \times 8 \times 2$ PT18β, and $2 \times 2 \times 1$ and $4 \times 4 \times 1$ PT75β elements are used. All the degrees of freedom on the clamped edges are restricted. Two cases are considered: (a) $a = 1$, $b = 1$, (b) $a = 1$, $b = 2$. For each of these cases, two subcases are considered: (i) $F = 4000$, $h = 0.02$, (ii) $F = 4$, $h = 0.002$. The Kirchoff plate theory-based solution for the displacement under the load is 0.05824 in the first case and 0.075088 in the second (for both subcases). The normalized results using these values are shown in

Table 1
Normalized tip deflections for the end-loaded straight and curved beams

	In-plane		Out-of-plane	
	PT18β	PT75β	PT18β	PT75β
Straight beam, mesh (a)	0.97340	0.99232	0.97347	0.99100
Straight beam, mesh (b)	0.04779	0.63094	0.02969	0.38097
Straight beam, mesh (c)	0.61320	0.95534	0.57886	0.92223
Curved beam	0.87631	1.00054	0.83124	0.94806

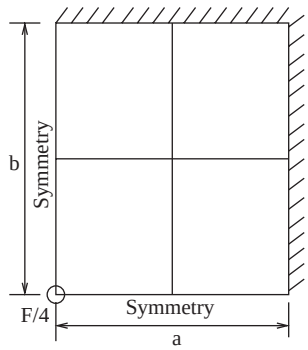

Fig. 5. Clamped rectangular plate problem; a quarter of the plate is shown modeled using PT75β with 5 nodes per side.

Table 2
Normalized center-point deflections for the clamped rectangular plate problem

	$a = 1, b = 1$				$a = 1, b = 2$			
	$h = 0.02$		$h = 0.002$		$h = 0.02$		$h = 0.002$	
Nodes/side	PT18β	PT75β	PT18β	PT75β	PT18β	PT75β	PT18β	PT75β
5	0.95156	0.98678	0.94857	0.98346	0.91695	0.97551	0.91470	0.97295
9	0.98625	0.99530	0.98269	0.99148	0.97526	0.99243	0.97264	0.98955

Table 2. Both the PT18β and PT75β elements seem to be immune to shear locking as the thickness of the plate is reduced. However, the PT18β element seems to suffer a greater loss in accuracy as the lateral aspect ratio of the element is increased.

3.4. Simply-supported circular plate

To further test whether the proposed elements are immune to shear locking, we consider a simply-supported circular plate of radius 10, and with $\nu = 0.3$, subjected to a unit pressure load on the top

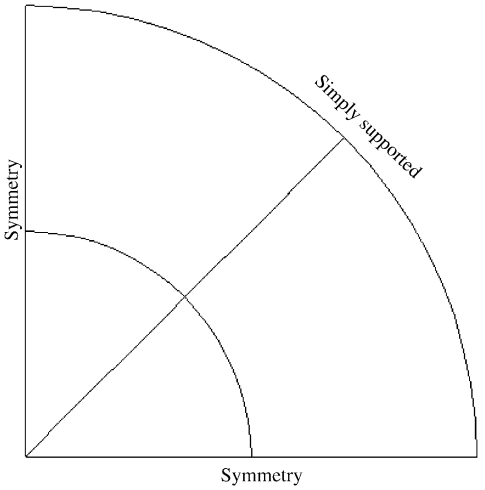

Fig. 6. Simply-supported circular plate subjected to uniform pressure; a quarter of the domain is shown modeled using a combination of W21/PT75β elements with 5 nodes per side.

Table 3
Normalized center-point displacements in the circular plate problem

Nodes/side	$h = 1$			$h = 0.01$		
	I21/I27	W6/PT18β	W21/PT75β	I21/I27	W6/PT18β	W21/PT75β
5	0.93092	0.94439	1.02086	0.12731	0.94735	1.02673
9	0.97705	0.98558	1.00055	0.64929	0.98902	0.97851
17	0.99418	0.99441	0.99751	0.88213	0.99779	0.97736

surface shown in Fig. 6. Two cases are considered: (i) $E = 10^4$, $h = 1$ ("thick plate"), and (ii) $E = 10^{10}$, $h = 0.01$ ("thin plate"). The analytical solutions for the center-point deflection are 0.70388 and 0.69563, respectively. The normalized results for the center-point deflection are presented in Table 3. As can be seen, both the developed elements are quite immune to shear-locking even when the thickness/radius ratio is as small as 1/1000.

3.5. Multilayer fibre-reinforced composite plate

The difficulties inherent in modeling laminated composites using either degenerated solid or classical shell theory-based elements are the following:

1. the use of rotational degrees of freedom in the geometrically exact stress-resultant formulations requires complex update procedures, and also requires the use of transition elements for connecting them to solid elements,

Table 4
Normalized center-point deflections for the laminated plate problem

Nodes/side	$\theta = 15^\circ$		$\theta = 45^\circ$	
	PT18β	PT75β	PT18β	PT75β
5	1.19656	1.51486	1.09902	1.31123
9	1.15224	1.17608	1.03313	1.03775
17	1.16862	1.17566	1.02874	1.02917

2. the zero transverse normal stress condition has to be imposed,
3. the accuracy of through the thickness stress distribution is poor,
4. the treatment of laminated composites with ply drop-offs, especially in shell structures can be quite complicated.

In contrast, the use of solid brick elements allows one to use complex 3-D constitutive relations, and also allows one to model thin or thick laminates since no special kinematic assumptions are made during the formulation. The only disadvantage of high computational cost can be alleviated if they are designed to yield accurate results even for large aspect ratios.

To get an idea of the accuracy of the results as a function of aspect ratio, consider a $20 \times 20 \times 0.02$ plate that is clamped along its lateral edges, and subjected to a uniformly distributed load of unit magnitude [7]. The plate is made of two layers with angle-ply $-\theta$ in the top layer and $+\theta$ in the bottom, and the material properties are $E_{11} = 40 \times 10^6$, $E_{22} = 10^6$, $\nu_{12} = \nu_{23} = 0.25$, and $G_{12} = G_{23} = 0.5 \times 10^6$; the expressions for the elements of the material compliance matrix $\boldsymbol{S}$ may be found in [16]. The analytical solutions for the center-point deflection (obtained using lamination theory) for $\theta = 15^\circ$ and 45° are 33.82 and 57.8, respectively. The results obtained using $4 \times 4 \times 4$, $8 \times 8 \times 4$ and $16 \times 16 \times 4$ meshes of PT18β elements, and $2 \times 2 \times 2$, $4 \times 4 \times 2$ and $8 \times 8 \times 2$ meshes of PT75β elements to model the entire plate are presented in Table 4. The solutions with the finest mesh for the $\theta = 45^\circ$ case are in good agreement with the analytical result for both types of elements inspite of the aspect ratio being 250! The solutions for the $\theta = 15^\circ$ case for both types of elements seem to be converging to a much higher value than the one predicted by the analytical solution; however, these results are in very good agreement with the results obtained by Spilker et al. [7] using an element formulation that is completely different from the one used here. Spilker et al. formulate their element so as to satisfy the traction boundary conditions at the upper and lower surfaces and at the layer interfaces exactly. In contrast, the weak implementation of these conditions has the advantage that no modification of the element formulation is required, and seems to have no adverse effect on the accuracy even for large aspect ratios.

As opposed to the results obtained on other example problems, the results obtained for the PT18β element using the coarsest mesh are far better than those obtained for the PT75β elements. The reason is that the weak implementation of the traction continuity condition at the interface makes the finite element model more "flexible"; on the other hand, the PT18β element is more stiffer than the PT75β element. Thus, there is a cancellation of these effects (which does not occur when the whole structure is of a single material) in the PT18β element leading to seemingly better results. Nevertheless, as is evident from Table 4, there is rapid convergence of the PT75β element results with successive refinements.

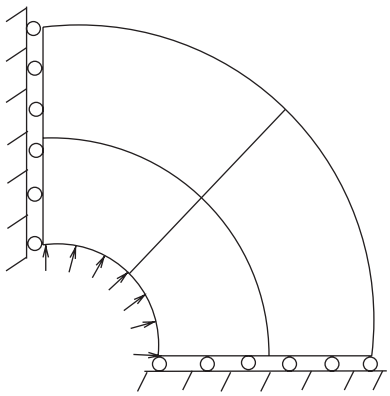

Fig. 7. Thick circular cylinder subjected to internal pressure; a quarter of the domain is shown modeled using PT75β elements with 5 nodes per side.

Table 5
Normalized radial displacement at the inner radius in the thick-cylinder problem; bracketed terms are corresponding values if the patch test requirement is not enforced

Nodes/side	$\nu = 0.499$		$\nu = 0.4999$	
	PT18β	PT75β	PT18β	PT75β
5	0.95973	0.95974 (0.96787)	0.95965	0.95972 (0.96787)
9	0.98888	0.99344 (0.99423)	0.98886	0.99344 (0.99423)
17	0.99714	0.99886 (0.99921)	0.99713	0.99886 (0.99921)

3.6. Thick-walled cylinder subjected to internal pressure

In addition to studying the effect of curved-edge distortion, this example also studies the performance of the PT75β when the material is almost incompressible, i.e., when $\nu \to 0.5$. A thick-walled circular cylinder of unit length, and inner radius 3 and outer radius 9 is subjected to a unit pressure at the inner radius under plane strain conditions. The material properties are $E = 1000$, and $\nu = 0.499$ or 0.4999. A quarter of the domain is modeled due to symmetry as shown in Fig. 7. Meshes of $4 \times 4 \times 2$, $8 \times 8 \times 2$ and $16 \times 16 \times 2$ PT18β, and $2 \times 2 \times 1$, $4 \times 4 \times 1$ and $8 \times 8 \times 1$ PT75β elements are used. The radial displacement at the inner radius, normalized against the exact solutions of 5.060249×10^{-3} (when $\nu = 0.499$) and 5.062275×10^{-3} (when $\nu = 0.4999$) are presented in Table 5; both the PT18β and PT75β elements yield good solutions even with coarse meshes as $\nu \to 0.5$. The solution for the stress components (τ_{rr}, $\tau_{\theta\theta}$, τ_{zz}) at point A on the inner surface, evaluated *directly* by means of Eq. (14a), and normalized against the analytical solution $(-1, 1.25, 0.12475)$ for the case when $\nu = 0.499$, is presented in Table 6. Although the displacement solutions are of comparable accuracy, the stresses obtained using the PT75β element are more accurate, especially on the coarsest mesh used.

Although, as seen from Table 6, the results for the τ_{rr} and $\tau_{\theta\theta}$ components increase in accuracy, those for the τ_{zz} component seem to be reducing in accuracy as the mesh is refined (although, of course, it

Table 6
Normalized stresses at the inner radius in the thick-cylinder problem; bracketed terms are corresponding values if the patch test requirement is not enforced

Nodes/side	τ_{rr}		$\tau_{\theta\theta}$		τ_{zz}	
	PT18β	PT75β	PT18β	PT75β	PT18β	PT75β
5	0.50344	0.87122 (0.94787)	1.12040	0.78070 (0.73457)	3.58824	0.88635 (0.50306)
9	0.73810	0.96086 (0.98027)	1.12867	0.91052 (0.88461)	2.69092	0.86163 (0.70878)
17	0.86481	0.99196 (0.99477)	1.08618	0.97262 (0.96031)	1.97168	0.84526 (0.77863)

is conceivable that this trend might reverse with further mesh refinement). This seems to be an artifact of using the Jacobian matrix to transform only the non-constant part of the stress tensor, which, as mentioned, was done in order to satisfy the patch test requirement. If one relaxes this requirement by using the Jacobian matrix to transform *all* the stress components (which, incidentally, is also the "correct" mathematical procedure), i.e., if one uses

$$\boldsymbol{P}_{(e)} = \left[\frac{1}{|\boldsymbol{J}_0|^{2/3}} \boldsymbol{A} \;\middle|\; \frac{1}{|\boldsymbol{J}_0|^{2/3}} \boldsymbol{A} \boldsymbol{N}_\tau \right] \tag{20}$$

instead of the expression in Eq. (17), then one obtains the bracketed results in Tables 5 and 6; note that, with this change, both the displacement and stress solutions converge to the analytical solution with mesh refinement. In all the other examples presented, except the coarsest mesh case for the pinched hemispherical shell problem, the differences in solutions obtained by the above modification in formulation are minor, and one can use either Eq. (17) or Eq. (20), depending on whether or not one wants to enforce the patch test requirement.

3.7. Twisted shell

A shell of length $L = 12$, width $w = 1.1$, thickness $h = 0.05$, and material properties $E = 29 \times 10^6$, $\nu = 0.22$, twisted by 90° is cantilevered and subjected to two cases of end loading (see Fig. 8):

a. unit shear load in the width direction,
b. unit shear load in the thickness direction.

All degrees of freedom at the cantilevered end are restricted. The results for the deflection in the direction of the load are normalized against the solutions 1.39 and 0.3431, respectively, and are presented in Table 7. Both the PT18β and PT75β elements yield good results, even with coarse meshes.

3.8. Pinched hemispherical shell

A hemisphere with and without an 18° hole at the top is subjected to pinching loads; only a quadrant is modeled due to symmetry as shown in Fig. 9. The properties are $E = 6.825 \times 10^7$, $\nu = 0.3$, mean radius

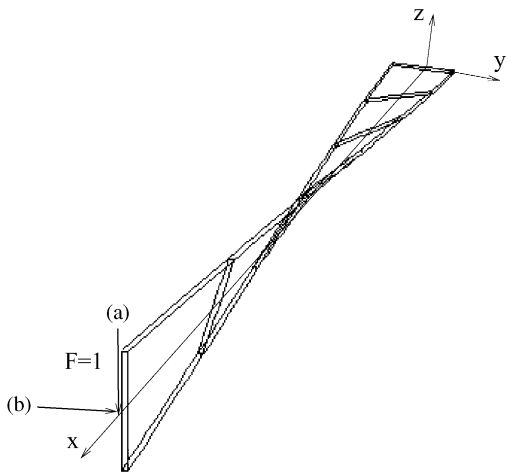

Fig. 8. A twisted shell subjected to a shear load (a) in the width direction, (b) in the thickness direction, shown modeled using PT75β elements with $13 \times 3 \times 3$ nodes.

Table 7
Normalized displacements in the twisted shell problem

Nodes/side	Load case (a)			Load case (b)		
	I27	PT18β	PT75β	I27	PT18β	PT75β
13×3	0.61823	0.98752	0.99530	0.62001	0.98612	1.00169
25×5	0.95189	0.99718	0.99821	0.95622	0.99911	1.00190
49×9	0.99470	0.99915	0.99937	0.99762	1.00123	1.00187

$R = 10$, and thickness $h = 0.04$. Meshes of $4 \times 4 \times 2$, $8 \times 8 \times 2$ and $16 \times 16 \times 2$ PT18β elements, and $2 \times 2 \times 1$, $4 \times 4 \times 1$ and $8 \times 8 \times 1$ PT75β elements are used in the case where the hemisphere has a hole; meshes with the same number of nodes per side are used for the full hemisphere case, with the layer near to the center of the hemisphere being modeled by wedge elements. The results for the displacement at the point of application of the forces, normalized against the solutions of 0.09355 and 0.0924, are presented in Table 8. Severe locking is observed with the isoparametric and lower-order hybrid elements on the coarsest mesh used, while a significantly better solution is obtained with the use of the proposed elements, especially with the use of the formulation in which the patch test requirement is not enforced (see bracketed terms in Table 8). Also note that the rate of convergence of the solution with the use of the proposed elements is very rapid.

3.9. Scordellis-Lo barrel vault

A short cylindrical section constrained by a rigid diaphragm at each end (see Fig. 10) is loaded by gravity forces given by $\boldsymbol{b} = -360\boldsymbol{e}_z$. The properties used are $E = 4.32 \times 10^8$, $\nu = 0$, thickness $h = 0.25$, mean radius $R = 25$, length $L = 50$, and half-span angle of the section $\theta = 40°$. Due to symmetry, a

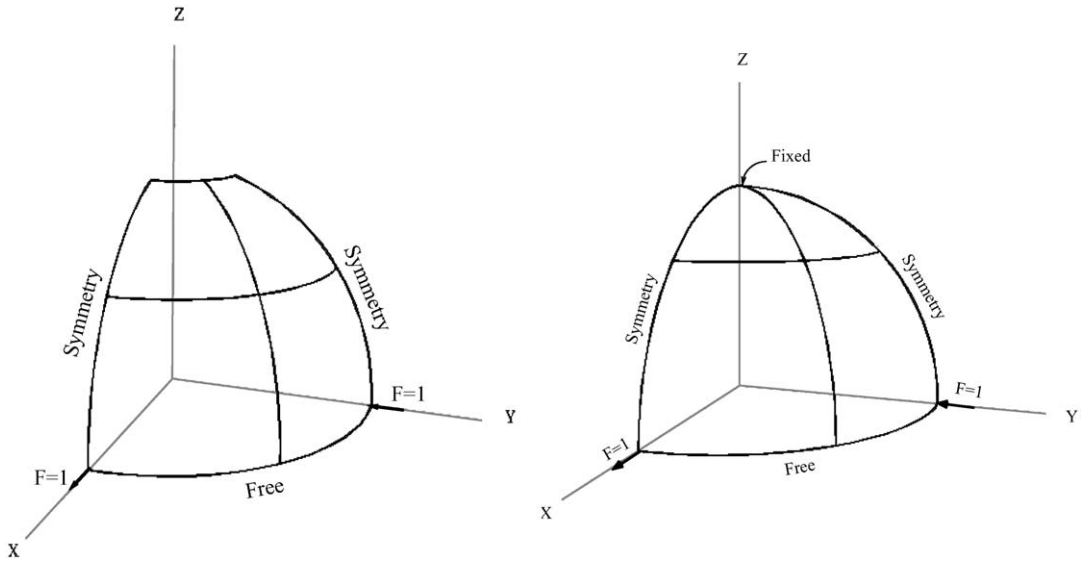

Fig. 9. Pinched hemispherical shell with and without an 18° hole; only a quadrant is modeled in both problems due to symmetry.

Table 8
Normalized displacements for the pinched hemisphere problem; bracketed terms are corresponding values if the patch test requirement is not enforced

Nodes/side	I27	PT18β	PT75β
Hemisphere with hole			
5	0.00146	0.04103	0.63315 (1.06313)
9	0.02174	0.74478	0.99882 (1.00501)
17	0.25715	0.98914	0.99945 (0.99899)
Hemisphere without hole			
Nodes/side	I21/I27	W6/PT18β	W21/PT75β
5	0.00104	0.01764	0.14534 (0.34241)
9	0.01474	0.38235	0.80872 (0.82454)
17	0.18373	0.95028	0.98546 (0.98475)

quadrant is modeled by meshes of $4 \times 4 \times 2$, $8 \times 8 \times 2$ and $16 \times 16 \times 2$ PT18β elements, and $2 \times 2 \times 1$, $4 \times 4 \times 1$ and $8 \times 8 \times 1$ PT75β elements. The vertical deflections at point A, normalized using the (numerically-obtained) solution of 0.3024, are listed in Table 9. Consistent with the results obtained using shell elements in [11], the solution seems to converge to a slightly lower value than the one used for normalization. Both, the PT18β and PT75β elements, yield good results even with coarse meshes.

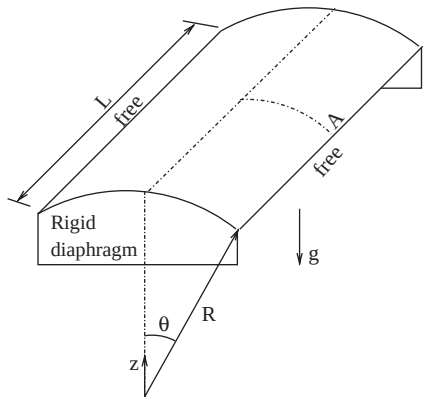

Fig. 10. Scordellis-Lo barrel vault problem setup.

Table 9
Normalized displacements for the Scordellis-Lo barrel vault problem

Nodes/side	I27	PT18β	PT75β
5	0.26502	1.02708	0.98745
9	0.81313	1.00456	0.99631
17	0.98046	0.99720	0.99661

3.10. Cylindrical shell subjected to pinching harmonic loads

The purpose of this example is to show that the PT75β formulation yields good results in vibration/transient analysis problems since the mass matrix (given by $\int_\Omega \rho \boldsymbol{N}^t \boldsymbol{N}\, \mathrm{d}\Omega$) is also computed very accurately in this formulation. A simply-supported cylindrical shell of length 0.2, mean radius 0.1, thickness 0.002, and with material properties $E = 20.6 \times 10^{10}$, $v = 0.3$, $\rho = 7850$ is subjected to two diametrically opposite pinching point loads $F = 10^3 \cos(10^4 t)$ at the midspan. Due to the symmetry of the structure and the loading, only one-eighth of the domain can be modeled as shown in Fig. 11. The analytical solution for the undamped steady-state amplitude of vibration is 6.571×10^{-5}, and is obtained by superposing the solutions for each individual load presented in [17] (see p. 212). The finite element solutions normalized against this value are presented in Table 10. Note that the normalized solutions obtained using the PT75β elements seem to be converging to a value higher than one. The reason is that the analytical solution has been obtained by neglecting both shear deformation and rotatory inertia, due to which the value of a natural frequency whose value is slightly greater than the driving frequency, and which contributes significantly to the solution, is overestimated, which in turn results in an underestimation of the response amplitude. Note also that, for the coarsest mesh, even the sign of the solution obtained with the PT18β elements is incorrect, and that a more accurate solution is obtained with the coarsest mesh of PT75β elements than the one obtained using the intermediate-level mesh of PT18β elements.

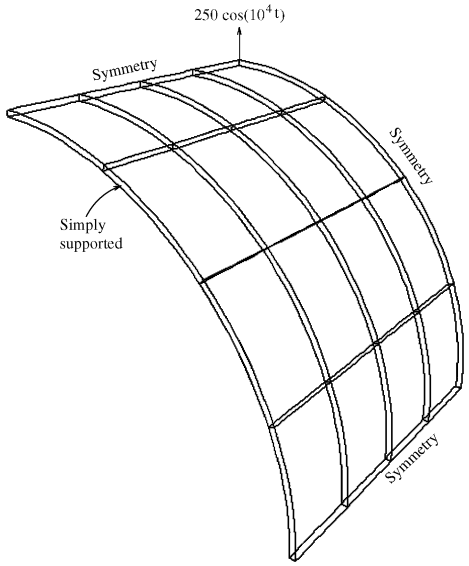

Fig. 11. Pinched cylinder problem; one-eighth of the domain is shown modeled using PT75β elements with 9 nodes per side.

Table 10
Normalized amplitudes of vibration for the pinched cylinder problem

Nodes/side	PT18β	PT75β
9	−2.28239	0.67024
17	0.45035	1.05816
33	0.93800	1.10414

4. Conclusions

The formulation and numerical results for a 27-node hybrid brick and a 21-node hybrid wedge element have been presented in this work. Ideally speaking, one would like an element to work well for shell/plate as well as fully three-dimensional problems, when the material is compressible or nearly incompressible, when the mesh is regular or distorted, and so on, all this of course without requiring a very fine discretization. Although the elements presented in this work do not completely satisfy all the above requirements, they do satisfy them to a large extent. Comparison with the PT18β element (for the same overall number of degrees of freedom) on several demanding problems reveals that the proposed PT75β element yields higher accuracy, especially in pathological problems such as ones involving trapezoidal meshes or doubly-curved shells, where the increase in accuracy is sometimes by as much as an order of magnitude. Although no special strategies have been used to eliminate shear or membrane locking (since they are not designed exclusively for plate/shell analysis), the proposed elements yield results that are only slightly inferior to those obtained using shell elements, and the convergence with mesh refinement to the exact solution is very rapid. The computational cost as compared to shell elements is higher, but what is gained is versatility in modeling a wide variety of geometries including three-dimensional ones

(which shell elements obviously cannot be used to model), and simplicity from a user viewpoint since only displacement degrees of freedom are used. The results obtained in modeling a multilayer composite with one element per ply in the thickness direction are also extremely encouraging, especially since (i) good results are obtained even for large aspect ratios, (ii) there is no change in the element formulation, whether one or multiple materials are involved, (iii) thin or thick laminates can be modeled since both elements are fully three-dimensional, with no a priori kinematic assumptions made during their formulation, (iv) ply drop-offs can be handled routinely.

Our numerical experiments indicate that relaxing patch test requirements can lead to comparable or even higher accuracy in some cases (as in the pinched hemispherical shell problem). This is consistent with the finding in [11], where it was shown that one can get a high performance element even though it may violate the patch test in a small way. In any case, the formulation for both versions, and some comparative results have been documented, so that a more detailed study of this issue can be carried out.

One of the criticisms that is leveled against hybrid elements, from which the proposed elements are not immune, is the high cost of forming the element stiffness matrix. However, we believe that instead of comparing the computational cost for a given number of degrees of freedom, the comparison ought to be between computational costs incurred to *achieve a given level of accuracy* on non-trivial problems, and from this viewpoint, since relatively far lesser number of hybrid elements are required, they are cheaper than conventional elements. Nevertheless, suggestions have been made in this work to reduce even this cost, so that it is negligible in comparison to the cost of solving the global finite element equations.

Extensions of the proposed elements to handle non-linear problems or other interesting applications such as, e.g., ones involving functionally graded materials, would obviously be of interest.

References

[1] W. Chen, Y.K. Cheung, Three-dimensional 8-node and 20-node refined hybrid isoparametric elements, Int. J. Numer. Meth. Eng. 35 (1992) 1871–1889.

[2] J.A.T. Freitas, F.L.S. Bussamra, Three-dimensional hybrid-Trefftz stress elements, Int. J. Numer. Meth. Eng. 47 (2000) 927–950.

[3] T.H. Pian, D. Chen, On the suppression of zero energy deformation modes, Int. J. Numer. Meth. Eng. 19 (1983) 1741–1752.

[4] R.L. Spilker, S.P. Singh, Three-dimensional hybrid-stress isoparametric quadratic displacement elements, Int. J. Numer. Meth. Eng. 18 (1982) 445–465.

[5] K.Y. Sze, Stabilization schemes for 12-node to 21-node brick elements based on orthogonal and consistently assumed stress modes, Comput. Meth. Appl. Mech. Eng. 119 (1994) 325–340.

[6] K.Y. Sze, W.K. Chan, T.H.H. Pian, An eight-node hybrid-stress solid-shell element for geometric non-linear analysis of elastic shells, Int. J. Numer. Meth. Eng. 55 (2002) 853–878.

[7] R.L. Spilker, B.E. Engelmann, Hybrid-stress isoparametric elements for moderately thick and thin multilayer plates, Comput. Meth. Appl. Mech. Eng. 56 (1986) 339–361.

[8] S.W. Lee, J.J. Rhiu, A new efficient approach to the formulation of mixed finite element models for structural analysis, Int. J. Numer. Meth. Eng. 23 (1986) 1629–1641.

[9] J.J. Rhiu, S.W. Lee, A new efficient mixed formulation for thin shell finite element models, Int. J. Numer. Meth. Eng. 24 (1987) 581–604.

[10] K.Y. Sze, A novel approach for devising higher-order hybrid elements, Int. J. Numer. Meth. Eng. 36 (1993) 3303–3316.

[11] C.S. Jog, Higher-order shell elements based on a Cosserat model, and their use in the topology design of structures, Comput. Meth. Appl. Mech. Eng. 193 (2004) 2191–2220.

[12] E.F. Punch, S.N. Atluri, Development and testing of stable, invariant, isoparametric curvilinear 2- and 3-d hybrid-stress elements, Comput. Meth. Appl. Mech. Eng. 47 (1984) 331–356.

[13] K.Y. Sze, X.H. Liu, S.H.H. Lo, Hybrid-stress six-node prismatic elements, Int. J. Numer. Meth. Eng. 61 (2004) 1451–1470.
[14] R.H. MacNeal, R.L. Harder, A proposed standard set of problems to test finite element accuracy, Finite Elem. Anal. Design 1 (1985) 3–20.
[15] T.H. Pian, P. Tong, Relations between incompatible displacement model and hybrid stress model, Int. J. Numer. Meth. Eng. 22 (1986) 173–181.
[16] R.L. Spilker, Hybrid-stress eight-node elements for thin and thick multilayer laminated plates, Int. J. Numer. Meth. Eng. 18 (1982) 801–828.
[17] W. Soedel, Vibrations of Shells and Plates, Marcel Dekker, New York, 1993.